Simulating Topographic Effects on Spaceborne Radiometric Observations Between L and X Frequency Bands

Nazzareno Pierdicca, *Member, IEEE*, Luca Pulvirenti, *Member, IEEE*, and Frank Silvio Marzano, *Senior Member, IEEE*

***Abstract*—A numerical simulator of satellite microwave-radiometric observations of orographically complex scenes, at various frequencies and observation angles, has been developed. The Simulator of Topographic Artefacts in MIcrowave RAdiometry (STAMIRA) exploits the information on the relief, extracted from a digital elevation model, and has been applied to a test case concerning a mountainous area in the Alps by assuming a simplified land-cover scenario consisting of bare terrain with two kinds of roughness (smooth and rough soils). The 1–10-GHz range has been considered to determine scattering and emission of soil and a nonscattering atmosphere has been supposed. The simulations have shown the large impact of the rotation of the polarization plane and of the brightness-temperature enhancement occurring for facets illuminated by radiation from the surrounding elevated terrain with respect to flat surfaces which scatter atmospheric downward radiation only. By considering also the antenna-pattern integration and the dependence of surface emissivity on the local observation angle, we have found that, for our case study, the brightness temperature is larger than that measured observing a flat terrain at horizontal polarization. At vertical polarization, the opposite occurs. These differences are analyzed and quantified.**

***Index Terms*—Microwave radiometry, relief, topography.**

I. Introduction

HILLY and mountainous areas represent important targets to be observed from satellites, particularly for hydrological purposes. Over these areas, the surface effective emission and the atmospheric contribution are considerably influenced by relief effects [1]. Quantifying these effects on the measurements of a spaceborne microwave radiometer is important because most of the algorithms developed to retrieve biogeophysical parameters, such as soil moisture, assume that the Earth surface is horizontal, so that their application for areas with complex topography may lead to significant errors.

Relief effects (i.e., surface roughness at pixel scale) influence the upwelling brightness temperature (T_B) measured by a satellite microwave radiometer in numerous ways [1], [2]. The atmospheric contributions are modified due to their dependence on the surface altitude; the downwelling atmospheric radiation can be shadowed, and radiation emitted by one tilted surface can be reflected by another one. The radiometer local observation angle is function of the surface slope and aspect, and a depolarization effect occurs, due to a rotation of the linear-polarization plane. Moreover, at microwave frequencies, the highly inhomogeneous features of the mountainous scenario should be compared with the relatively large antenna footprints [3].

In [1], Mätzler and Standley investigated the topography effects for microwave radiometry over land, particularly focusing on the shadowing of sky radiation by an elevated horizon. They stated that a pixel illuminated by the radiation coming from neighbors located at higher altitude increases its T_B with respect to a pixel that scatters atmospheric downward radiation only. This increase was computed by assuming that the elevated surface was a blackbody at constant temperature and for a Lambertian scattering surface.

The influence of the relief was also considered in [2], [4], and [5]. These investigations concerned the L-band Soil Moisture and Ocean Salinity (SMOS) instrument (using aperture synthesis) only. In [2], the level of topography influencing the radiometric signal was assessed, while in [4] it has been shown that, for the region of Catalonia (Spain), the maximum variations of local incidence angle due to topography can reach 55°.

In a previous paper [3], we quantified the effect of the modification of the local observation angle and of the rotation of the plane of linear polarization, due to the relief, on the emitted component of the upwelling brightness temperature. Moreover, we produced an approximated evaluation of the impact of these effects on soil-moisture retrieval because the study concerned frequency channels devoted to this application.

In this paper, we aim at producing a complete quantification of the topographic effects on the spaceborne microwave-radiometric measurements thus complementing the previous studies on this topic. For this purpose, we have developed a software package named Simulator of Topographic Artefacts in MIcrowave RAdiometry (STAMIRA) that is able to operate at various microwave frequencies and observation angles.

While the atmospheric contribution is accounted for through a radiative-transfer scheme already validated (e.g., [6]) and the thermal-emission contribution is computed as in [3], the original aspect of this paper is mainly represented by the

Manuscript received October 1, 2008; revised February 13, 2009 and June 3, 2009. First published October 9, 2009; current version published December 23, 2009.

The authors are with the Department of Electronic Engineering, Sapienza University of Rome, 00184 Rome, Italy (e-mail: nazzareno.pierdicca@uniroma1.it; pulvirenti@die.uniroma1.it; marzano@die.uniroma1.it).

Color versions of one or more of the figures in this paper are available online at http://ieeexplore.ieee.org.

Digital Object Identifier 10.1109/TGRS.2009.2028881

consideration of the downwelling radiation scattered by the surface. Its calculation, in the presence of a complex relief, is a fairly complicated task because the downwelling radiation is originated either from the sky or from the elevated landscape, depending on the horizon. In addition, the bistatic-scattering behavior of the surface has to be modeled. This paper is mainly focused on the representation of both coherent and incoherent components of surface scattering and on the approach for determining the horizon and for discriminating radiation of the elevated terrain from sky radiation.

The relief effects are quantified for a simple case study in which the land cover is supposed to be bare soil with two kinds of roughness (smooth and rough surfaces). To perform the simulation, we have exploited a digital elevation model (DEM) of Italy, and we have focused on the Alpine region and its surroundings. The 1–10-GHz frequency range has been considered, and we have assumed two radiometer configurations characterized by a conical scan.

In Section II we give a description of the various procedures used to determine the components of the radiation at satellite level that are included in the simulator. Section III analyzes the results of our study, and Section IV draws the main conclusions.

II. Simulator

The numerical simulation of a radiometric observation of a mountainous area is based on the following formula, which expresses the P-polarized upwelling $T_B(T_{BP})$, where P may be H (horizontal) or V (vertical), measured by a satellite radiometer as

$$T_{BP} = (T_{\mathrm{em}P} + T_{\mathrm{sc}P})t + T_{\mathrm{up}} \tag{1}$$

where $T_{\mathrm{em}P}$ is the P-polarized emitted component, t is the atmospheric transmittance, T_{up} is the atmospheric upwelling radiation, and $T_{\mathrm{sc}P}$ is the P-polarized downwelling radiation scattered by the considered surface. In the following, we illustrate the computation of the various terms of (1) implemented in STAMIRA.

A. Atmospheric Parameters

STAMIRA includes two relationships, which express the trend of the radiative effective emitting temperature T_{mr} (weighted-average profile temperature) of the atmosphere and of the atmospheric optical thickness τ versus the surface altitude z (derived from the DEM). The functional forms of these relationships depend on frequency. To infer them, we have first used a radiative-transfer scheme, assuming a plane-parallel nonscattering atmosphere [6], which has allowed us to compute both T_{mr} and τ from a set of vertical profiles of temperature, pressure, and relative humidity, obtained from meteorological analysis fields provided by the European Centre for Medium-Range Weather Forecasts (ECMWF). Note that, for the sake of simplicity, the upwelling and downwelling T_{mr} have been supposed equal and the extraterrestrial T_B has been approximated to the cosmic background ($T_{\cos} = 2.75$ K) at all the frequencies. Supposing a single narrow-band receiver, the following relations apply

$$t = e^{-\tau/\mu} \tag{2a}$$

$$T_{\mathrm{up}} = T_{\mathrm{mr}}(1-t) \tag{2b}$$

$$T_{\mathrm{sky}} = T_{\mathrm{mr}}(1-t) + T_{\cos}t \tag{2c}$$

where μ is the cosine of the observation angle and T_{sky} is the sky radiation.

Considering that, in a mountainous zone, the atmospheric contributions depend on the surface altitude, we have computed the T_{mr} and τ values for various surface heights and at different times in order to derive their mean trend versus z. The spatial sampling extends over an Alpine zone of 128 $\times$ 128 km (the same considered in [3], whose limits are $45.9^\circ - 47.0^\circ$ N, $7.7^\circ - 9.4^\circ$ E). As for the temporal sampling, the ECMWF analysis fields have been collected throughout the first ten days of each month of year 2000. Then, we have fitted the trends with a polynomial relationship to determine the expected atmospheric contribution of each DEM element as a function of its height. For the X-band, we have used a second-degree polynomial for T_{mr} and a first-degree polynomial for τ, while at the C- and L-bands, the atmosphere is almost transparent in nonscattering conditions [7], with very small values of τ almost constant in the range of surface heights. Note that, although in this study we apply our simulator to the 1–10-GHz frequency range, we foresee extending the use of STAMIRA at higher frequencies too, where the atmosphere is far from being transparent, even in the absence of scattering phenomena.

B. Emitted Component

STAMIRA includes a module for the computation of $T_{\mathrm{em}P}$ that is based on the study carried out in [3]. For each DEM element, this module derives the aspect and the slope angles and determines the local surface normal. Then, it calculates the angle between the surface normal and the radiometer-observation direction, i.e., the local observation angle θ_l, and the angle between the polarization-basis vectors in the global coordinate system (related to the direction of observation) and in the local coordinate system (related to the surface element), that is, the rotation angle of the polarization plane ψ. Note that the radiometer-observation direction is not a constant term in the simulator (see [3]), since a conical scanning is conceived with constant zenith angle but varying azimuth.

To compute the emissivity of a facet of the DEM as a function of θ_l, a model should be used. A semiempirical relationship that is widely adopted to express the P-polarized emissivity of bare soil (e_P) has the following form (e.g., [7]–[10]):

$$e_P(\theta_l) = 1 - \left[\Gamma_P^{\mathrm{sp}}(\theta_l)(1-q_s) - q_s\Gamma_Q^{\mathrm{sp}}(\theta_l)\right]\exp(-h_s). \tag{3}$$

In (3), q_s is the polarization coupling factor, h_s is a parameter related to the surface roughness (at wavelength scale), while Γ_P^{sp} and Γ_Q^{sp} are the P- and Q-polarized (either H, or V) specular Fresnel reflectivities (one minus the emissivities). Several estimates for q_s and h_s were provided in the literature for various frequencies, which are generally derived from experimental data.

To accomplish this study, we have chosen the q_s and h_s values provided by the investigation of Wang *et al.* [8] (hereafter, the Wang model) because they concern L-, C-, and X-bands. $\Gamma_H^{\rm sp}$ and $\Gamma_V^{\rm sp}$ have been evaluated by applying the soil-permittivity model by Dobson *et al.* [11]. We have considered a terrain characterized by fairly standard values of volumetric moisture (0.25) and dry-soil density (1.3 g/m^3), while the fractions of sand and clay have been assumed equal to 32% and 25%, respectively, and two values of standard deviation of the surface height s, i.e., $s = 0.73$ cm (smooth soil) and $s = 2.45$ cm (rough soil) have been used to describe the bare-soil roughness (as in [8]).

After the calculation of e_P as a function of θ_l, this parameter has to be referenced to the global coordinate system through [3]

$$e'_P(\theta_l, \psi) = e_P(\theta_l)\cos^2\psi + e_Q(\theta_l)\sin^2\psi. \tag{4}$$

Denoting by T_s the soil temperature of a certain DEM element at height z, the emitted component of the P-polarized T_B at satellite level is

$$T_{{\rm em}P} = e'_P(\theta_l, \psi)T_s(z). \tag{5}$$

While in [3] we made the simplifying hypothesis of a constant soil temperature T_s, STAMIRA assumes that T_s decreases with z according to a standard temperature gradient of 6.5 K/km. T_s has been supposed constant with depth in the soil, over the range of penetration of the considered frequencies, and the temperature at sea level ($z = 0$) has been supposed to be 296 K.

C. Radiation Scattered by the Surface

While the computation of the atmospheric parameters and of the emitted component relies on previous studies [3], [6], the algorithm to calculate $T_{{\rm sc}P}$ in the presence of a complex topography is the most distinctive aspect of this work.

The problem requires the knowledge of the soil bistatic-scattering coefficient. For the sake of computation efficiency, STAMIRA describes the surface bistatic-scattering behavior at P-polarization through a combination of a specular coherent component and a term depending on the cosine of the scattering zenith angle θ_s, representing the diffuse incoherent component. The cosinusoidal dependence on θ_s makes the incoherently scattered radiance independent of the scattering direction, in relatively good agreement with the trend of the bistatic-scattering coefficient versus θ_s (for a given incidence angle) that we have assessed in [12] by exploiting a well-established physical model, such as the Advanced Integral Equation Model (AIEM) [13]. With this simplifying assumption, considering the local coordinate system, the sum σ_P^0 of the copolarized (σ_{PP}^0) and cross-polarized (σ_{PQ}^0) components of the bistatic-scattering coefficient is given by

$$\sigma_{PP}^0 + \sigma_{PQ}^0 = \sigma_P^0 = (1-\alpha)\sigma_{0P}^0(\theta_l)\cos\theta_s + \alpha\frac{4\pi\Gamma_P^{\rm sp}\cos\theta_l}{\sin\theta_{\rm sp}}\delta(\theta_s - \theta_{\rm sp})\delta(\varphi_s - \varphi_{\rm sp}) \tag{6}$$

where θ_l, in this case, is the incidence angle in the local frame, δ is the Dirac function, $\theta_{\rm sp}$ and $\varphi_{\rm sp}$ denote the zenith and azimuth angles corresponding to the specular direction, respectively, α, spanning the interval [0, 1], represents the specularity factor, and the quantity σ_{0P}^0 describes the dependence of the incoherent component on θ_l. Note that the dependence of σ_{PP}^0 and σ_{PQ}^0 on $(\theta_l, \theta_s; \varphi_l, \varphi_s)$ has been omitted from the notation for conciseness.

While in (3) θ_l is the direction from which the emissivity is observed, σ_P^0 relates the magnitude of the power scattered in the direction (θ_s, φ_s) to the power incident from (θ_l, φ_l) (see [14]). This apparently different meaning of θ_l between (3) and (6) is due to the application of the Kirchhoff's radiation law [14] which states that $e_P(\theta_l)$ is equal to one minus the reflectivity $\Gamma_P(\theta_l)$. To determine $\Gamma_P(\theta_l)$, σ_P^0 must be integrated over $d\Omega_s = \sin\theta_s d\theta_s d\varphi_s$, and divided by $4\pi\cos\theta_l$. Performing the same kind of integration for the product $T_{\rm sky}\sigma_P^0$, it is also possible to calculate $T_{{\rm sc}P}(\theta_l)$, as will be shown later on [see (9)].

The result of the integration of σ_P^0 over the upper hemisphere is

$$\Gamma_P(\theta_l) = 1 - e_P(\theta_l) = \frac{1}{4\pi\cos\theta_l}\int_{2\pi}\sigma_P^0 d\Omega_s = \frac{(1-\alpha)\sigma_{0P}^0(\theta_l)}{4\cos\theta_l} + \alpha\Gamma_P^{\rm sp}(\theta_l) = (1-\alpha)\Gamma_P^{\rm in} + \alpha\Gamma_P^{\rm sp}(\theta_l). \tag{7}$$

In (7), we have put $\Gamma_P^{\rm in} = \sigma_{0P}^0(\theta_l)/(4\cos\theta_l)$, where the superscript *in* indicates that this quantity originates from the incoherent component of the bistatic-scattering coefficient. To make $\Gamma_P(\theta_l)$ consistent with the expression of $e_P(\theta_l)$ given by (3), we have found the following:

$$\alpha = (1 - q_s)\exp(-h_s) \tag{8a}$$

$$\Gamma_P^{\rm in} = q_s\Gamma_{0Q}\exp(-h_s)/(1-\alpha). \tag{8b}$$

Note that in this way, the amplitude of the coherent component contains a factor $\exp(-h_s)$, thus, being in agreement with well-known relationships (e.g., scalar approximation of the Physical Optics formulation, see [15]) accounting for a factor equal to $\exp(-4k_0^2\cos^2\theta_l s^2)$, which attenuates the specular coherent component for increasing roughness (k_0 is the wavenumber). Moreover, to verify reciprocity, $\Gamma_P^{\rm in}$ should not depend on θ_l, so that an average over the range 0°–90° has been carried out.

Once both the coherent and incoherent components of the surface reflectivity are known, we can express the downwelling brightness temperature scattered by a facet of the DEM $T_{{\rm sc}P}$ [see (1)] that (in the local frame) is given by [14]

$$T_{{\rm sc}P}(\theta_l) = \frac{1}{4\pi\cos\theta_l}\int_{2\pi}\sigma_P^0 T_{\rm sky}(\theta_s)d\Omega_s. \tag{9}$$

Note that, as mentioned in Section II-A, we have supposed a plane-parallel atmosphere so that $T_{\rm sky}$ does not depend on the azimuth angle.

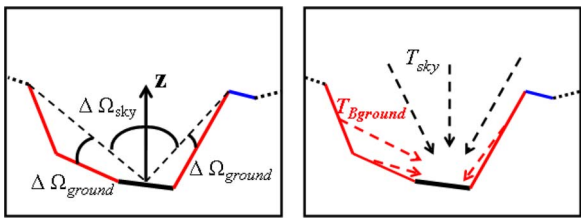

Fig. 1. Various contributions to $T_{\mathrm{sc}P}$. Left panel shows the horizon of a surface element and the corresponding solid angles under which the element sees the $(\Delta\Omega_{\mathrm{ground}})$ elevated landscape and $(\Delta\Omega_{\mathrm{sky}})$ the sky. Right panel shows the components of the brightness-temperature incident upon the surface coming from $(T_{B\mathrm{ground}})$ below and (T_{sky}) above the horizon.

In the presence of relief, each surface element (an individual cell of the DEM) may diffuse both the sky radiation and the radiation from the elevated landscape. Moreover, when substituting the expression of σ_P^0 in (9), it has to be considered that $\cos\theta_s$ is given by $\mathbf{n}\cdot\mathbf{m}$, i.e., by the scalar product between the unit vector $\mathbf{n}$ denoting the surface normal and that representing the direction from which the radiation impinges on the surface. By indicating with $\Delta\Omega_{\mathrm{ground}}$ the solid angle under which each individual facet observes the surrounding terrain, with $\Delta\Omega_{\mathrm{sky}}$ the corresponding quantity for the sky radiation, and accounting for (6)–(8), we can write

$$T_{\mathrm{sc}P} = \alpha\Gamma_P^{\mathrm{sp}} T_{\mathrm{sp}} + (1-\alpha)\left(\Gamma_P^{\mathrm{in}}/\pi\right) \times \left[\int_{\Delta\Omega_{\mathrm{ground}}} T_{B_{\mathrm{ground}}}(\theta_s,\varphi_s,z)[\mathbf{n}\cdot\mathbf{m}]d\Omega_s + \int_{\Delta\Omega_{\mathrm{sky}}} T_{\mathrm{sky}}(\theta_s,z)[\mathbf{n}\cdot\mathbf{m}]\mathrm{d}\Omega_s\right]. \quad (10)$$

In (10), T_{sp} is the brightness temperature coming from the specular direction (either from the sky, or from an elevated surface, depending on the horizon) being coherently reflected, while $T_{B\mathrm{ground}}$ is the downwelling T_B coming from below the horizon. Fig. 1 explains the geometry.

The term within the square brackets in (10) is proportional to the irradiance incident on the surface. To discriminate between the irradiance due to the elevated terrain [first integral of (10)] and sky radiation (second integral), as well as to determine the horizon of every DEM facet, we have implemented inside STAMIRA a module based on a sort of ray-tracing algorithm.

We have considered a moving window centered around each facet, so that the rays originate from the center and their length depends on the dimension of the window, as shown in the upper panel of Fig. 2, in which black lines mark grid boxes, while blue and red lines mark radiation paths. In particular, red lines cross pixels that are visible from the central one, while a blue line crosses hidden pixels. To make the central element of the window clearly identifiable, the rays crossing it are not drawn in the figure.

The central and bottom panels of Fig. 2 show the way STAMIRA finds the horizon of each path and discriminates

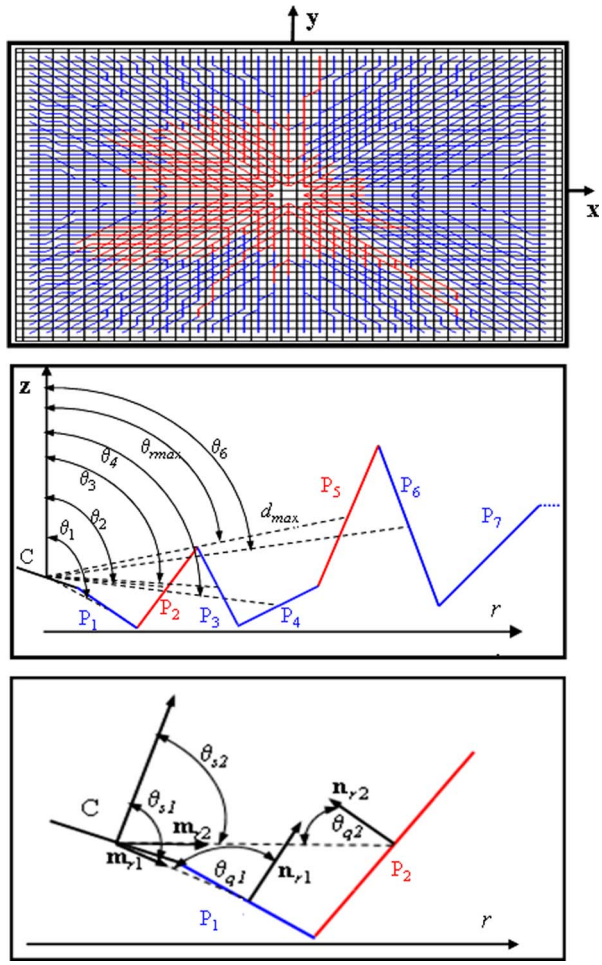

Fig. 2. Ray-tracing algorithm applied to a moving window surrounding each DEM cell. Upper panel shows the paths between the center and the edge of the window. Black lines mark grid boxes, blue and red lines mark radiation paths crossing either (blue lines) hidden facets or (red lines) visible facets. Central and lower panels illustrate the evaluation of the horizon for each path and the discrimination of (red) visible DEM elements from (blue) hidden ones. Note that z is the vertical axis, while the axes x and y define the horizontal plane. See text for details.

visible (blue) and hidden (red) facets. In these panels, r identifies the rth ray ($r = 1 : N_r$, where N_r denotes the number of paths between the center and the edge of the window) and P_k indicates the kth facet crossed by the ray ($k = 1 : N_{rk}$, where N_{rk} denotes the number of pixel crossed by the rth ray). In this way, the dependence of unit vector $\mathbf{m}$ on (θ_s,φ_s), omitted from the notation of (10) for conciseness, is replaced by that on (r,k), and the symbol $\mathbf{m}_{rk}$ is used in the figure to make explicit this dependence (see bottom panel).

First, STAMIRA scans the central coordinates of the DEM cells along the ray to search for the zenith angle of the horizon $\theta_{r\max}$ and identifies the corresponding pixel (the peripheral facet P_5 in the example of the central panel of Fig. 2), whose distance from the central one (C) is indicated as $d_{\max}$. Facets whose distance from C is larger than $d_{\max}$ (P_6 and P_7, in the example) are not visible. Then, STAMIRA performs a scan of the other pixels along the considered ray (distances that are less than or equal to $d_{\max}$): let us indicate as $\theta_k(k = 1 : N_{kr})$ the angle between the vertical axis (z) and the line connecting C with $\mathrm{P}_k(\overline{\mathrm{CP}}_k)$, with $\theta_{sk}(k = 1 : N_{kr})$ the angle between

the normal to C ($\mathbf{n}$) and $\mathbf{m}_{rk}$ (see bottom panel where the central one is zoomed considering only C, P_1, and P_2), and with $\theta_{qk}(k = 1 : N_{kr})$ the angle between the normal to $\mathrm{P}_k(\mathbf{n}_k)$ and $\overline{\mathrm{CP}}_k$ (see bottom panel). The kth peripheral facet is visible if all the following three conditions are verified: 1) $\theta_k < \theta_h$ $(h = 1 : k-1)$; 2) $\theta_{sk} < 90^\circ$; and 3) $\theta_{qk} < 90^\circ$.

It can be observed that, in the example of Fig. 2, P_1 is not visible (blue) because $\theta_{q1} > 90^\circ$. The same applies for P_3 that is oriented in the same way as P_1 with respect to C (θ_{q3} is not shown for conciseness), while P_4 is hidden because θ_4 is larger than θ_2 and θ_3. It is worth noting that θ_k is given by the sum of θ_{sk} plus the slope angle of C. The computations of θ_{sk} and θ_{qk} are described in Appendix A.

Once STAMIRA has established that a peripheral pixel is visible from the central one, it calculates the T_B emitted by the former toward the latter (i.e., $T_{B\mathrm{ground}}$, which is a function of θ_{qk}) and the solid angle under which the central facet observes the peripheral one $\Delta\Omega_{\mathrm{ground}}(r,k)$. All the contributions originating from the elevated terrain are finally summed, so that the first integral in (10) has been approximated as

$$I_1 = \sum_{r=1}^{N_r}\sum_{k=1}^{N_{rk}} [T_{\mathrm{ground}}(r,k,z)(\mathbf{n}\cdot\mathbf{m}_{rk})\Delta\Omega_{\mathrm{ground}}(r,k)] \quad (11)$$

where the polarizations are not indicated for conciseness and $T_{B\mathrm{ground}}$ has been evaluated as in (5), so that it depends on the surface altitude z. To sum all the contributions from the elevated landscape, they have been referenced to the local coordinate system of the central pixel. Successively, $T_{\mathrm{sc}P}$ has been referenced to the global frame [see (4)].

To calculate the irradiance due to sky radiation, it must be considered that, for each ray, sky radiation is limited to the incidence angles between 0° and $\theta_{r\max}$ (see Fig. 2, central panel) so that the second integral in (10) can be approximated as

$$I_2 = \sum_{r=1}^{N_r}\left[\Delta\varphi_r \int_0^{\theta_{r\max}} T_{\mathrm{sky}}(\theta_s,z)\,[\mathbf{n}\cdot\mathbf{m}_r(\theta_s)]\,d\theta_s\right]. \quad (12)$$

In (12), $\Delta\varphi_r$ represents the increment of the azimuth angle between two adjacent rays, and T_{sky} has been computed through (2a) and (2c). With respect to (11), one integral has not been approximated through a sum because it can be computed in closed form, so that instead of $\mathbf{m}_{rk}$, we use the notation $\mathbf{m}_r(\theta_s)$. The integral has been tabulated for several values of $\theta_{r\max}$ and z in order to speed up the computation. Note that $\theta_{r\max}$ in the absolute frame is upper limited by the maximum zenith angle of $\pi/2$ in the local frame.

Before ending this section, the computation of the specular component T_{sp} in (10) has to be illustrated. According to the relationships written in Appendix B, STAMIRA adopts a "reverse ray tracing" and determines the DEM element in the specular direction $\mathbf{s}_{\mathrm{sp}}$ with respect to the observation direction, represented by the versor $\mathbf{s}_i$, as shown in Fig. 3. Versor $\mathbf{s}_{\mathrm{sp}}$ can be represented also by the zenith angle θ_{sp} and the azimuth angle φ_{sp} in the absolute frame (see Appendix B). Azimuth φ_{sp} defines, in the window centered on the element, the ray that has to be examined to determine whether T_{sp} comes from

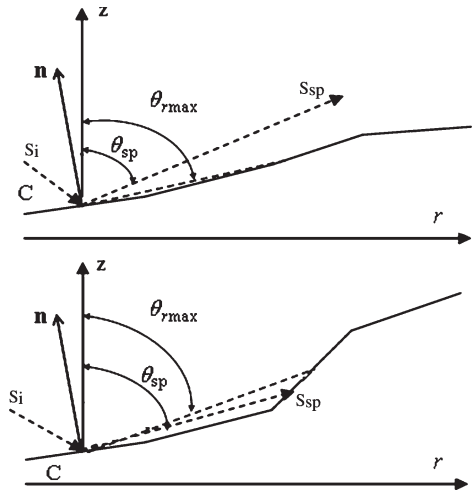

Fig. 3. Specular direction denoted by versor $\mathbf{s}_{\mathrm{sp}}$, while $\mathbf{s}_i$ represents the looking direction. Upper and lower panels show the cases in which the radiation coming from specular direction is originated from the sky and from the ground, respectively.

the sky or from the elevated landscape (the rth ray in Fig. 3). For this ray, if $\theta_{\mathrm{sp}} < \theta_{r\max}$ (upper panel of Fig. 3), sky radiation is reflected, otherwise, the specular reflection concerns brightness temperature emitted from the ground (lower panel of Fig. 3). In the former case, T_{sp} has been computed through (2a) and (2c), while in the latter case, as in (5) and depends on polarization.

The computation of the number N of DEM elements comprised in every radiometric pixel, i.e., in the instantaneous field of view (IFOV) of the radiometer antenna, and the evaluation of the antenna temperature has been finally accomplished by making the same simplifying hypotheses as in [3], except for the estimation of the pixels affected by shadowing in the antenna footprint, which has been performed as in [4]. We have supposed, for simplicity, that the antenna is characterized by major lobe efficiency equal to one and by a constant directivity D within the major lobe. Indicating by θ_{ni} the slope angle of the ith element of the DEM included in the considered radiometric pixel, by θ_{li} its local observation angle, and by T_{BPi} its brightness temperature, the antenna temperature T_P (again, P represents polarization) has been approximated as [3]

$$T_P = \frac{\sum_{i=1}^{N} T_{BPi} D\Omega_i}{\sum_{i=1}^{N} D\Omega_i} = \frac{\sum_{i=1}^{N} T_{BPi} D\frac{A\cos\theta_{li}}{H^2\cos\theta_{ni}}}{\sum_{i=1}^{N} D\frac{A\cos\theta_{li}}{H^2\cos\theta_{ni}}} = \frac{\sum_{i=1}^{N} T_{BPi}\frac{\cos\theta_{li}}{\cos\theta_{ni}}}{\sum_{i=1}^{N}\frac{\cos\theta_{li}}{\cos\theta_{ni}}}. \quad (13)$$

In (13), A is the area of a DEM element referenced to a projection on the horizontal plane so that its actual area is given by $(A/\cos\theta_{ni})$, while Ω_i is the solid angle under which the ith facet is observed by the radiometer that is equal to $(A\cos\theta_{li}/H^2\cos\theta_{ni})$, H being the range from the DEM cell to the satellite, which is constant, assuming a conical scanning, a narrow beam, and neglecting the cell height with respect to the satellite height (see [3]).

III. Numerical Results

To perform the quantification of the relief effects, we have focused our analysis on a mountainous area in the Alps (Northern Italy), and we have derived the topography from a DEM of Italy having a spatial resolution of 250 × 250 m. We have simulated the radiometric image for three frequency bands: 1.4, 6.9, and 10.6 GHz by assuming a conically scanning sensor. For the latter two bands, we have made reference to the Advanced Microwave Scanning Radiometer for the Earth Observing System (AMSR-E) [16], supposing a sensor observing the Earth at 55° from an altitude of 705 km. In this case, the following spatial resolutions have been supposed: 75 × 43 km for C-band and 51 × 29 km for X-band [16]. For L-band (1.4 GHz), we have considered an instrument characterized by an observation angle of 40° and orbiting at 670 km of altitude, as that foreseen for the radiometer aboard the future Soil Moisture Active Passive (SMAP) mission [17]. A spatial resolution of 40 × 40 km has been assumed.

For the AMSR-E-like scan, we have considered a portion of 512 × 512 elements of the DEM (i.e., 128 × 128 km) as in [3]. This portion, comprising a wide range of topography (the height standard deviation is ∼800 m and the slope standard deviation is ∼11°), includes 63 radiometric pixels at C-band and 99 at X-band, if a radiometric pixel spacing of 10 × 10 km [16] is assumed. Regarding the L-band simulation, we have supposed a radiometric pixel spacing on the order of the dimension of the pixel itself, so that we have enlarged the area (1024 × 512 elements, i.e., 256 × 128 km), thus including 21 radiometric pixels. A further widening of the area would have implied a very high computational time.

The results of the AMSR-E-like and SMAP-like simulations will be discussed by making reference to two quantities. The first one is $T_P - T_{P\_\mathrm{flat}}$, which is the difference between the antenna temperature calculated through (13) and that computed for a flat terrain (having the same roughness, moisture, and composition) located at an altitude equal to the average of the heights of the DEM facets within the antenna IFOV. The term $T_P - T_{P\_\mathrm{flat}}$ permits the evaluation of the topographic effects at subpixel scale on spaceborne radiometric observations, which is the objective of this work. The second quantity is the corresponding one for the emitted component only, i.e., $T_{\mathrm{em}P} - T_{\mathrm{em}P\_\mathrm{flat}}$. Plots of $T_P - T_{P_{\mathrm{flat}}}$ versus $T_{\mathrm{em}P} - T_{\mathrm{em}P\_\mathrm{flat}}$ will be shown in Sections III-A and III-B to single out both tilting effects on the emitted component and the effect of the shadowing of sky radiation on the scattered component.

A. Results for C- and X-bands

Fig. 4 shows the results of our simulation exercise obtained for the 6-GHz and 10-GHz frequency bands and for a rough soil ($s = 2.45$ cm). It can be noted that all the points are located above the principal diagonal (dashed line), i.e., $T_P - T_{P\_\mathrm{flat}} > T_{\mathrm{em}P} - T_{\mathrm{em}P\_\mathrm{flat}}$. Moreover, at horizontal polarization (H-pol), both $T_P - T_{P\_\mathrm{flat}}$ and $T_{\mathrm{em}P} - T_{\mathrm{em}P\_\mathrm{flat}}$ are positive quantities, while the opposite occurs at V-pol.

The results are shown in Table I, which reports the average values of $T_P - T_{P\_\mathrm{flat}}$ and $T_{\mathrm{em}P} - T_{\mathrm{em}P\_\mathrm{flat}}$, computed over the 63 points for C-band and 99 for X-band considered in Fig. 4. It includes the case of a smooth soil ($s = 0.73$ cm), too.

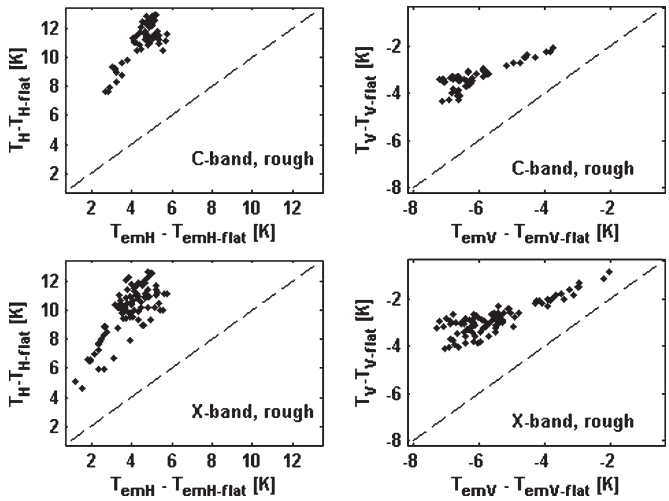

Fig. 4. $T_P - T_{P\_\mathrm{flat}}$ versus $T_{\mathrm{em}P} - T_{\mathrm{em}P\_\mathrm{flat}}$ for a rough soil ($s = 2.45$ cm). (Left panels) H polarization. (Right panels) V polarization. (Upper panels) C-band. (Lower panels) X-band.

TABLE I
Average Values [K] of $T_P - T_{P\_\mathrm{flat}}$ and $T_{\mathrm{em}P} - T_{\mathrm{em}P\_\mathrm{flat}}$

	C-band rough	*X-band rough*	*C-band smooth*	*X-band smooth*
$\overline{T_H - T_{H\_flat}}$	11.2	10.0	18.6	16.0
$\overline{T_{emH} - T_{emH\_flat}}$	4.6	3.9	12.9	9. 9
$\overline{T_V - T_{V\_flat}}$	-3.3	-2.8	-12.6	-9.6
$\overline{T_{emV} - T_{emV\_flat}}$	-6.1	-5.5	-15.6	-12.5

The results for the emitted component were analyzed in detail in [3]. Although in [3] a different emissivity model [18] was used and the dependence of surface temperature on height was neglected, the positive impact of variable terrain on the emitted component at H-pol (i.e., $T_{\mathrm{em}H} - T_{\mathrm{em}H\_\mathrm{flat}} > 0$) and the negative one at V-pol are supported in this study, too, so that the analyses we made to explain this behavior still apply. To briefly summarize those findings, the values of $T_{\mathrm{em}P} - T_{\mathrm{em}P\_\mathrm{flat}}$ are mainly determined by: 1) dependence of emissivity on local observation angle θ_l; 2) rotation of the polarization plane; and 3) antenna-pattern integration. As for the dependence on θ_l, the emissivity decreases with the increase of θ_l, except for a smooth soil at V-pol. In this case, the decrease occurs for θ_l larger than the Brewster angle, as shown in Fig. 5. The coupling of the polarizations causes an increase of the emissivity at H-pol and a decrease at V-pol. The beam-weighted integration due to the antenna tends to raise the antenna temperature at H-pol because, according to the Wang model, the facets with the highest emissivity are those whose θ_{li} is small (see Fig. 5). Since for these facets, $(\cos\theta_{li}/\cos\theta_{ni})$ is large [see (13)], they appear to the radiometer under a larger solid angle. As for V-pol, the facets producing the highest emission are observed at the Brewster angle, where $(\cos\theta_{li}/\cos\theta_{ni})$ is relatively small.

The increase of $T_P - T_{P\_\mathrm{flat}}$ with respect to $T_{\mathrm{em}P} - T_{\mathrm{em}P\_\mathrm{flat}}$ indicates that $T_{\mathrm{sc}P}$ (scattered component of the T_B at satellite level) in the presence of the relief is larger than

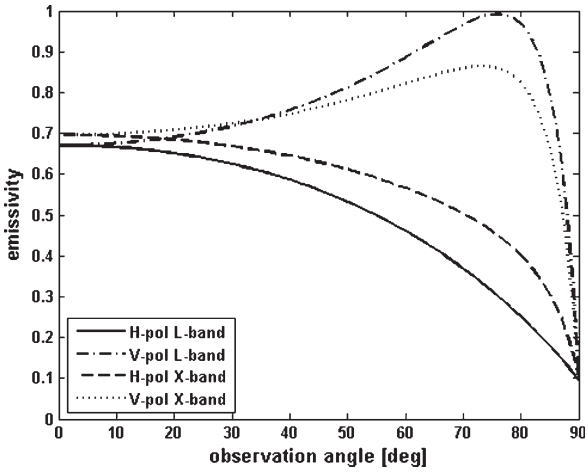

Fig. 5. Emissivity versus observation angle for a smooth soil ($s = 0.73$ cm) according to the Wang model [8].

the corresponding quantity computed for a horizontal surface [see (1)]. Although according to (1), T_{BP} depends on the atmospheric variables too, making reference to T_{P_flat} and $T_{\mathrm{em}P\_\mathrm{flat}}$ evaluated at the average height of the radiometric pixel, the effects of height dependence on temperature and atmospheric parameters are mitigated in Fig. 4, and the subpixel topography effect is singled out.

The increase of $T_{\mathrm{sc}P}$ occurring in the presence of a complex topography can be explained by considering that surfaces illuminated by radiation from surrounding elevated terrain enhance their T_B with respect to the facet scattering atmospheric downward radiation only [1], since $T_{B\mathrm{ground}}$ is larger than T_{sky}. At V-pol, the increase of the scattered component due to the radiation of the elevated landscape does not compensate for the decrease of the emitted component, so that $T_V - T_{V\_\mathrm{flat}} < 0$. Conversely, at H-pol, this increase is added to that due to the emitted component. In other words, the scattering contribution enhances the positive impact of a variable terrain on the brightness temperature at H-pol, whereas it mitigates the negative impact at V-pol. From Table I, we can observe that the difference between $\overline{T_P - T_{P\_\mathrm{flat}}}$ and $\overline{T_{\mathrm{em}P} - T_{\mathrm{em}P\_\mathrm{flat}}}$ is actually larger at H-pol (between 5.7 and 6.6 K) than at V-pol (around 3 K).

The different behavior of scattering at the two linear polarizations originates from a combination of the polarization mixing of the incident (from surrounding elevated terrain) and scattered radiation [see (4)] and of the difference between horizontal and vertical reflectivities.

It must be considered that, according to the Wang model, the emissivity/reflectivity for a smooth soil is considerably polarized around 55° (see Fig. 5). The use of a model predicting a less polarized emissivity/reflectivity would imply a smaller difference between $\overline{T_P - T_{P\_\mathrm{flat}}}$ and $\overline{T_{\mathrm{em}P} - T_{\mathrm{em}P\_\mathrm{flat}}}$. For example, by using in STAMIRA the expression for q_s given by Kerr and Njoku [7] and the value of h_s used by Wang and Choudhury [9], i.e., $(2k_0 s)^2$, the emissivity values for small observation angles (less than 40°) are close to one ($\sim$0.95). Consequently, we have obtained, for $s = 0.73$ cm at C-band, values of the mean differences considerably smaller than those we got with the Wang model. The previous considerations

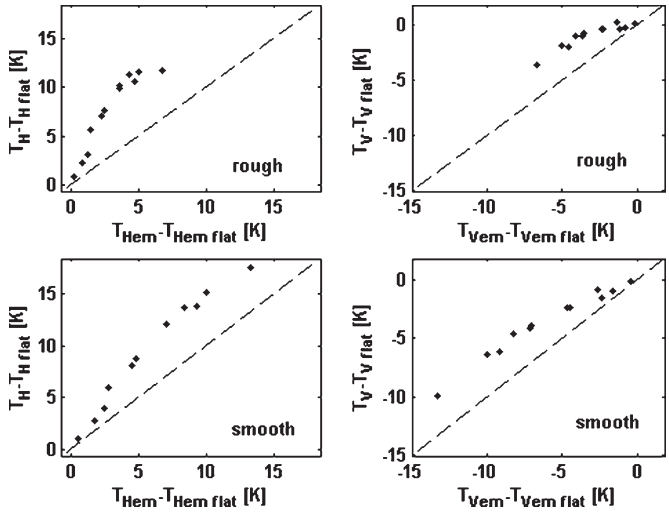

Fig. 6. $T_P - T_{P\_\mathrm{flat}}$ versus $T_{\mathrm{em}P} - T_{\mathrm{em}P\_\mathrm{flat}}$ for L-band. (Left panels) H polarization. (Right panels) V polarization. (Upper panels) Rough soil. (Lower panels) Smooth soil.

TABLE II
SAME AS TABLE I BUT FOR L-BAND

	rough	*smooth*
$\overline{T_H - T_{H\_flat}}$	8.3	10.8
$\overline{T_{emH} - T_{emH\_flat}}$	3.6	7.0
$\overline{T_V - T_{V\_flat}}$	-1.3	-4.5
$\overline{T_{emV} - T_{emV\_flat}}$	-3.5	-7.0

suggest that the topographic effect is also dependent on the type of surface cover.

B. Results for L-Band

The retrieval of biogeophysical parameters, such as soil moisture, from measurements at L-band is assuming great importance because of the future launches of the SMOS Mission [19] and of SMAP. It is therefore worthwhile to evaluate the relief effects at L-band, too. As mentioned, STAMIRA simulates a conical scan, consistent with SMAP specifications [17]. The results for the SMAP-like simulation of a radiometric image is shown in Fig. 6 and quantified in Table II.

In this case also, all the points are above the main diagonal. However, the difference between $\overline{T_P - T_{P\_\mathrm{flat}}}$ and $\overline{T_{\mathrm{em}P} - T_{\mathrm{em}P\_\mathrm{flat}}}$ is smaller, being 4.7 K for a rough soil and 3.8 K for a smooth soil at H-pol. At V-pol, this difference is $\sim$2 K. This decrease with respect to the corresponding quantity at C- and X-bands is mainly due to the fact that we are considering the SMAP observation angle, that is, local angles on the order of 40°. In this range, the difference between the emissivities at H- and V-pol is smaller than that around 55° (see Fig. 5). The aforementioned considerations explain also why the absolute values of $\overline{T_{\mathrm{em}P} - T_{\mathrm{em}P\_\mathrm{flat}}}$ are not as large as those found at 6 and 10 GHz. It is worth noting that the L-band emissivity at H-pol is less than that at higher frequencies (see Fig. 5), while, according to the Wang model, around 40°, the emissivity at V-pol does not depend very much on frequency in the range of 1–10 GHz.

IV. Summary and Conclusion

A simulator of radiometric images of a terrain with complex topography, named STAMIRA, has been developed in order to evaluate the influence of the relief on spaceborne microwave-radiometric observations. The frequency range 1–10-GHz, where the impact of the dependence of the atmospheric contributions on the altitude is fairly small, has been considered. The study has been particularly focused on the scattered component of the downwelling radiation that may be originated either from the sky or from the elevated landscape. In particular, we have concentrated our interest on some electromagnetic aspects of the problem, that is, the bistatic-scattering behavior of the surface, the way to take into account the coherent reflection and on the approach for determining the horizon and for discriminating visible and hidden portions of the surface.

Major effects are those due to the polarization coupling and to the fact that facets illuminated by radiation from surrounding elevated terrain enhance the brightness temperature with respect to surfaces which scatter atmospheric downward radiation only. These effects have been quantified for a simplified scenario in which the land cover has been assumed to be bare soil. We have found that, at horizontal polarization, the brightness temperature is larger than that measured observing a flat terrain. This difference, at C- and X-bands, in average, may exceed 15 K for very smooth soils whose surface emission is strongly polarized, according to the selected emission model. At L-band, the difference has been quantified between 8.3 K (rough soil) and 10.8 K (smooth soil). Conversely, at vertical polarization, the large impact of the polarization coupling implies that the brightness temperature is smaller than that measured observing a flat terrain. This decrease is partly compensated by the increase of the scattered brightness temperature due to the surrounding elevated terrain.

Using STAMIRA, we have shown that disregarding the terrain roughness at subpixel scale (i.e., the topography within the IFOV) may lead to relevant discrepancies between surface properties (e.g., soil moisture, temperature) and corresponding radiometric observations. This paper is therefore intended as providing a contribution to find a reliable road to account for these discrepancies in an error budget when attempting to estimate geophysical parameters from microwave radiometric images. The future of this research will concern the development of an approach to mitigate these errors within an inversion scheme. Such approach will include additional factors, such as vegetation cover, soil temperature depending on solar illumination, and moisture profiles to be applied to actual scenarios.

Appendix A
Radiation From the Elevated Landscape

Let us consider (11), which basically represents the irradiance on a surface element due to the surfaces below the horizon, and let us refer to the situation shown in Fig. 7, in which a notation coherent with that used in Fig. 2 is adopted, so that C is the central DEM facet and P_k, which illuminates C, is the kth peripheral facet crossed by the considered ray (the rth one). $T_{B\mathrm{ground}}$ (due to P_k) is given by the soil temperature multiplied

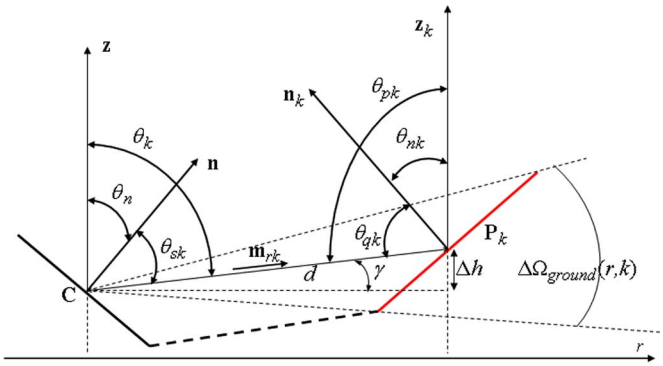

Fig. 7. Parameters involved in the computation of (11).

by the emissivity of P_k. To compute the latter, the angle θ_{qk} between $\mathbf{n}_k$ and $\overline{\mathrm{CP}}_k$, has to be calculated. It is given by

$$\begin{aligned}\mathbf{n}_k \cdot (-\mathbf{m}_{rk}) = \cos\theta_{qk} &= \sin\theta_{nk}\cos\varphi_{nk}\sin\theta_{pk}\cos\varphi_{pk} \\ &+ \sin\theta_{nk}\sin\varphi_{nk}\sin\theta_{pk}\sin\varphi_{pk} \\ &+ \cos\theta_{nk}\cos\theta_{pk} \\ &= \sin\theta_{nk}\sin\theta_{pk}\cos(\varphi_{nk}-\varphi_{pk}) \\ &+ \cos\theta_{nk}\cos\theta_{pk} \qquad \text{(A1)}\end{aligned}$$

where θ_{nk} and φ_{nk} are the slope and aspect of facet P_k, respectively, computed from the DEM and θ_{pk} is the angle between the vertical axis and $\overline{\mathrm{CP}}_k$, given by $90^\circ + \gamma = 90^\circ + \sin^{-1}(\Delta h/d)$. φ_{pk} is the azimuth angle under which the peripheral facet sees the central one, d is the distance between C and P_k, and Δh is the difference between their heights.

By adopting the same trigonometric relationship used to write the equality between the third and fourth members of (A1), the quantity $\mathbf{n}\cdot\mathbf{m}_{rk}$ in (11) can be expressed as (see Fig. 7)

$$\mathbf{n}\cdot\mathbf{m}_{rk} = \cos\theta_{sk} = \sin\theta_n\sin\theta_k\cos(\varphi_n-\varphi_k) + \cos\theta_n\cos\theta_k. \qquad \text{(A2)}$$

In (A2), θ_n and φ_n are the slope and aspect of facet C, respectively, θ_k is given by $90^\circ - \gamma$, and φ_k is the azimuth angle under which the central facet sees the peripheral one (φ_k differs from φ_{pk} by 180°). Finally, the solid angle under which P_k is seen by C has to be evaluated. If A indicates the area of a DEM element referenced to a projection on the horizontal plane [see (13)], this angle is expressed by [3]

$$\Delta\Omega_{\mathrm{ground}}(r,k) = \frac{A\cos\theta_{qk}}{d^2\cos\theta_{nk}} \qquad \text{(A3)}$$

where the definition of d is derived from Fig. 7. It is worth noting that (A2) applies also to calculate the quantity $\mathbf{n}\cdot\mathbf{m}(\theta_s)$ in (12). In this case, $\mathbf{m}(\theta_s)$ is identified by the integration variable θ_s and by the azimuth angle φ_{sp} corresponding to the considered ray (see the main text). The two quantities, (A1) and (A2), together with $\theta_k = \theta_n + \theta_{sk}$ are also used to discriminate the DEM elements which contribute to illuminate the central one from hidden facets, as explained in Section II-C.

APPENDIX B
SPECULAR DIRECTION

To determine the specular direction for each DEM element, represented by the versor $\mathbf{s}_{\rm sp}$, we make reference to Fig. 3. $\mathbf{s}_i$ is the versor representing the pointing direction (i.e., from the antenna to the DEM element). It is equal to $-\mathbf{o}$, where $\mathbf{o}$ denotes the direction pointing toward the radiometer, so that

$$\mathbf{o} = \mathbf{x}_0 \sin\theta_0 \cos\varphi_0 + \mathbf{y}_0 \sin\theta_0 \sin\varphi_0 + \mathbf{z}_0 \cos\theta_0 \qquad \text{(B1)}$$

where $\mathbf{x}_0$, $\mathbf{y}_0$, $\mathbf{z}_0$ are the unit vectors of the Cartesian system (absolute frame) and θ_0 and φ_0 are the zenith and azimuth angles, respectively, identifying the radiometer position. The specular versor $\mathbf{s}_{\rm sp}$ can be expressed as

$$\mathbf{s}_{\rm sp} = \mathbf{s}_i - 2(\mathbf{n} \cdot \mathbf{s}_i)\mathbf{n}. \qquad \text{(B2)}$$

Once $\mathbf{s}_{\rm sp}$ is known, the zenith angle $\theta_{\rm sp}$ and the azimuth angle $\varphi_{\rm sp}$ identifying $\mathbf{s}_{\rm sp}$ are easy to determine

$$\theta_{\rm sp} = \cos^{-1}(\mathbf{z}_0 \cdot \mathbf{s}_{\rm sp}) \qquad \text{(B3)}$$

$$\varphi_{\rm sp} = \sin^{-1}\left(\frac{\mathbf{x}_0 \cdot \mathbf{s}_{\rm sp}}{\sin\theta_{\rm sp}}\right). \qquad \text{(B4)}$$

Based on (B3) and (B4) relations, STAMIRA discriminates between land or sky contribution to the illumination and, as in the first case, identifies the contributing DEM element.

REFERENCES

[1] C. Mätzler and A. Standley, "Technical note: Relief effects for passive microwave remote sensing," *Int. J. Remote Sens.*, vol. 21, no. 12, pp. 2403–2412, Aug. 2000.

[2] Y. H. Kerr, F. Secherre, J. Lastenet, and J. P. Wigneron, "SMOS: Analysis of perturbing effects over land surfaces," in *Proc. IEEE IGARSS*, Jul. 2003, vol. 2, pp. 908–910.

[3] L. Pulvirenti, N. Pierdicca, and F. S. Marzano, "Topographic effects on the surface emissivity of a mountainous area observed by a spaceborne microwave radiometer," *Sensors*, vol. 8, no. 3, pp. 1459–1474, Mar. 2008.

[4] M. Talone, A. Camps, A. Monerris, M. Vall-Ilossera, P. Ferrazzoli, and M. Piles, "Surface topography and mixed-pixel effects on the simulated L-band brightness temperatures," *IEEE Trans. Geosci. Remote Sens.*, vol. 45, no. 7, pp. 1996–2003, Jul. 2007.

[5] M. J. Sandells, I. J. Davenport, and R. J. Gurney, "Passive L-band microwave soil moisture retrieval error arising from topography in otherwise uniform scene," *Adv. Water Resour.*, vol. 31, pp. 1433–1443, 2008.

[6] L. Pulvirenti and N. Pierdicca, "Retrieval of atmospheric and surface parameters from satellite microwave radiometers over the Mediterranean Sea," *IEEE Trans. Geosci. Remote Sens.*, vol. 44, no. 1, pp. 90–101, Jan. 2006.

[7] Y. H. Kerr and E. G. Njoku, "A semi empirical model for interpreting microwave emission from semiarid land surfaces as seen from space," *IEEE Trans. Geosci. Remote Sens.*, vol. 28, no. 3, pp. 384–393, May 1990.

[8] J. R. Wang, P. E. O'Neill, T. J. Jackson, and E. T. Engman, "Multifrequency measurements of the effects of soil moisture, soil texture and surface roughness," *IEEE Trans. Geosci. Remote Sens.*, vol. GRS-21, no. 1, pp. 44–51, Jan. 1983.

[9] J. R. Wang and B. J. Choudhury, "Remote sensing of soil moisture content over bare field at 1.4 GHz frequency," *J. Geophys. Res.*, vol. 86, no. C6, pp. 5277–5282, 1981.

[10] C. Prigent, J. P. Wigneron, W. B. Rossow, and J. R. Pardo-Carrion, "Frequency and angular variations of land surface microwave emissivities: Can we estimate SSM/T and AMSU emissivities from SSM/I emissivities," *IEEE Trans. Geosci. Remote Sens.*, vol. 38, no. 5, pp. 2373–2386, Sep. 2000.

[11] M. C. Dobson, F. T. Ulaby, M. T. Hallikainen, and M. El-Rayes, "Microwave dielectric behavior of wet soil—Part II: Dielectric mixing models," *IEEE Trans. Geosci. Remote Sens.*, vol. GRS-23, no. 1, pp. 35–46, Jan. 1985.

[12] N. Pierdicca, L. Pulvirenti, F. Ticconi, and M. Brogioni, "Radar bistatic configurations for soil moisture retrieval: A simulation study," *IEEE Trans. Geosci. Remote Sens.*, vol. 46, no. 10, pp. 3252–3264, Oct. 2008.

[13] K. S. Chen, T.-D. Wu, L. Tsang, Q. Li, J. Shi, and A. K. Fung, "Emission of rough surfaces calculated by the integral equation method with comparison to three-dimensional moment method simulations," *IEEE Trans. Geosci. Remote Sens.*, vol. 41, no. 1, pp. 90–101, Jan. 2003.

[14] F. T. Ulaby, R. K. Moore, and A. K. Fung, *Microwave Remote Sensing, Active and Passive*, vol. 1. Reading, MA: Addison-Wesley, 1981.

[15] F. T. Ulaby, R. K. Moore, and A. K. Fung, *Microwave Remote Sensing, Active and Passive*, vol. 2. Reading, MA: Addison-Wesley, 1982.

[16] T. Kawanishi, T. Sezai, Y. Ito, K. Imaoka, T. Takeshima, Y. Ishido, A. Shibata, M. Miura, H. Inahata, and R. W. Spencer, "The Advanced Microwave Scanning Radiometer for the Earth Observing System (AMSR-E), NASDA's contribution to the EOS for global energy and water cycle studies," *IEEE Trans. Geosci. Remote Sens.*, vol. 41, no. 2, pp. 184–194, Feb. 2003.

[17] D. Entekhabi, E. G. Njoku, P. E. O'Neill, T. J. Jackson, J. K. Entin, and I. Eastwood, "The Soil Moisture Active/Passive Mission (SMAP)," in *Proc. IEEE IGARSS*, Boston, MA, Jul. 2008, pp. III-1–III-4.

[18] U. Wegmüller and C. Mätzler, "Rough bare soil reflectivity model," *IEEE Trans. Geosci. Remote Sens.*, vol. 37, no. 3, pp. 1391–1395, May 1999.

[19] Y. H. Kerr, P. Waldteufel, J.-P. Wigneron, J.-M. Martinuzzi, J. Font, and M. Berger, "Soil moisture retrieval from space: The Soil Moisture and Ocean Salinity (SMOS) mission," *IEEE Trans. Geosci. Remote Sens.*, vol. 39, no. 8, pp. 1729–1735, Aug. 2001.

Nazzareno Pierdicca (M'04) was born in Rome, Italy, on June 11, 1954. He received the Laurea (Doctor's) degree in electronic engineering (*cum laude*) from Sapienza University of Rome, Italy, in 1981.

During 1978–1982, he was with the Italian Agency for Alternative Energy (ENEA), performing research and development activities in the field of thermal and mechanical behavior of nuclear fuel rods. From 1982 to 1990, he was with the Remote Sensing Division, Telespazio, Rome, Italy. He was involved and was responsible in various projects concerning remote-sensing applications, data interpretation, and ground-segment design. He was a Principal Investigator of the ESA/JRC Agrisar'86 airborne campaign and a Coinvestigator of the X-SAR/SIR-C experiment. Since November 1990, he has been with the Department of Electronic Engineering, Sapienza University of Rome, where he is currently an Associate Professor in the Faculty of Engineering and teaches remote sensing and antennas. He has been an Investigator of the MAC Europe'91 and X-SAR/SIR-C experiments. His research activity mainly concerns electromagnetic-scattering models, microwave radiometry of the atmosphere, and SAR land applications.

Prof. Pierdicca is the Chairman of the Geoscience and Remote Sensing Society (Central Italy Chapter).

Luca Pulvirenti (M'07) received the Laurea degree in electronic engineering and the Ph.D. degree in electromagnetism from Sapienza University of Rome, Italy, in 1999 and 2004, respectively.

He is currently a Postdoctoral Researcher with the Department of Electronic Engineering, Sapienza University of Rome, where, in 2007 and 2008, he taught electromagnetic propagation. His research interests include microwave remote sensing of the atmosphere and the Earth's surface, electromagnetic-scattering models of rough surfaces (in particular, bare soil and sea), microwave radiometry of the atmosphere, and inversion of electromagnetic forward models to retrieve soil parameters.

Dr. Pulvirenti is a member of the Italian Society of Electromagnetism (SiEM) and the Italian Association of Remote Sensing (AIT).

Frank Silvio Marzano (S'89–M'99–SM'03) received the Laurea degree (*cum laude*) in electrical engineering and the Ph.D. degree in applied electromagnetics from Sapienza University of Rome, Italy, in 1988 and 1993, respectively.

In 1993, he collaborated with the Institute of Atmospheric Physics, CNR, Rome, Italy. From 1994 until 1996, he was with the Italian Space Agency, Rome, Italy, as a Postdoctoral Researcher. After being a Lecturer with the University of Perugia, Perugia, Italy, in 1997, he joined the Department of Electrical Engineering and cofounded the Center of Excellence (CETEMPS), University of L'Aquila, L'Aquila, Italy, coordinating the Satellite and Radar Remote Sensing Laboratory. Since 2005, he has been with the Department of Electronic Engineering, Sapienza University of Rome, Italy, where he currently teaches courses on antennas and remote sensing. He has published more than 65 papers in international refereed journals and more than 120 extended abstracts in conference proceedings. His current research concerns passive and active remote sensing of the atmosphere from ground-based, airborne, and spaceborne platforms, with a particular focus on precipitation using microwave and infrared data, development of inversion methods, radiative transfer modeling of scattering media, and radar meteorology issues. He is also involved in radiopropagation topics in relation to incoherent-wave modeling, scintillation prediction, and rain-fading analysis along satellite microwave links.

Dr. Marzano is a member of the Italian Society of Electromagnetics (SiEM). He received the Young Scientist Award of XXIV General Assembly of the International Union of Radio Science (URSI) in 1993. In 1998, he was the recipient of the Alan Berman Publication Award (ARPAD) from the Naval Research Laboratory, Washington, DC. From 2001, he was the Italian national delegate for the European COST actions n. 720 on atmospheric profiling by ground-based remote sensing and n. 280 on satellite-fade mitigation techniques. Since January 2004, he has been acting as an Associate Editor of the IEEE GEOSCIENCE REMOTE SENSING LETTERS. In 2004 and 2006, he was a Co-Guest Editor of the special issues on MicroRad for the IEEE TRANSACTIONS ON GEOSCIENCE AND REMOTE SENSING.